PNAS RESEARCH ARTICLE | EARTH, ATMOSPHERIC, AND PLANETARY SCIENCES OPEN ACCESS

The Bering Strait was flooded 10,000 years before the Last Glacial Maximum

Jesse R. Farmer[a,b,1], Tamara Pico[c,1], Ona M. Underwood[a], Rebecca Cleveland Stout[d,2], Julie Granger[e], Thomas M. Cronin[f], François Fripiat[b,g], Alfredo Martínez-García[b], Gerald H. Haug[b,h], and Daniel M. Sigman[a]

Edited by Claire Waelbroeck, Laboratoire d'Océanographie et du Climat: Expérimentations et Approches Numériques, Institut Pierre-Simon Laplace, Paris, France; received April 18, 2022; accepted October 21, 2022 by Editorial Board Member Jean Jouzel

The cyclic growth and decay of continental ice sheets can be reconstructed from the history of global sea level. Sea level is relatively well constrained for the Last Glacial Maximum (LGM, 26,500 to 19,000 y ago, 26.5 to 19 ka) and the ensuing deglaciation. However, sea-level estimates for the period of ice-sheet growth before the LGM vary by > 60 m, an uncertainty comparable to the sea-level equivalent of the contemporary Antarctic Ice Sheet. Here, we constrain sea level prior to the LGM by reconstructing the flooding history of the shallow Bering Strait since 46 ka. Using a geochemical proxy of Pacific nutrient input to the Arctic Ocean, we find that the Bering Strait was flooded from the beginning of our records at 46 ka until $35.7^{+3.3}_{-2.4}$ ka. To match this flooding history, our sea-level model requires an ice history in which over 50% of the LGM's global peak ice volume grew after 46 ka. This finding implies that global ice volume and climate were not linearly coupled during the last ice age, with implications for the controls on each. Moreover, our results shorten the time window between the opening of the Bering Land Bridge and the arrival of humans in the Americas.

Arctic Ocean | Bering Strait | sea level | foraminifera-bound N isotopes | glacial isostatic adjustment

Significance

The Bering Strait was a land bridge during the peak of the last ice age (the Last Glacial Maximum, LGM), when sea level was ~130 m lower than today. This study reconstructs the history of sea level at the Bering Strait by tracing the influence of Pacific waters in the Arctic Ocean. We find that the Bering Strait was open from at least 46,000 until 35,700 y ago, thus dating the last formation of the land bridge to within 10,000 y of the LGM. This history requires that ice volume increased rapidly into the LGM. In addition, it appears that humans migrated to the Americas as soon as the formation of the land bridge allowed for their passage.

The Bering Strait, the ~53 m deep ocean passage that separates Asia from North America (1), is the only Northern Hemisphere connection between the Pacific and Atlantic Oceans. Today, ~1 Sv (10^6 m^3 s^{-1}) of low-salinity Pacific seawater flows northward across the Bering Strait (2) and contributes to the relative freshness of the upper Arctic Ocean (Fig. 1). Export of these Arctic waters into the subpolar North Atlantic modifies the surface waters that form North Atlantic Deep Water (3) and may cause feedbacks between the North Pacific and North Atlantic Oceans (4–6).

During the last glacial cycle, sea-level changes driven by the growth and decay of continental ice sheets exposed and flooded the Bering Strait. The Bering Strait flooded most recently between 13 and 11 ka during sea-level rise caused by the melting of ice sheets (11, 12). Before 13 ka, the Bering Strait was subaerially exposed due to lowered sea level from extensive continental ice sheets during the Last Glacial Maximum (LGM) (26.5 to 19 ka, ref. (13)) and early deglaciation. At this time, Asia and North America were connected by the Bering Land Bridge, a proposed route by which human populations first entered the Americas (14–16). However, there is great uncertainty as to the timing with which ice growth leading up to the LGM exposed the Bering Strait and formed the Bering Land Bridge. Hopkins (14) initially reported geological evidence for Bering Strait submergence prior to the LGM, but this evidence is debated (17).

Relative sea level at the Bering Strait (RSL_{BeSt}) is affected by global mean sea level (GMSL) and the solid Earth response to the growth and decay of ice sheets through the process of glacial isostatic adjustment (11). Uncertainty regarding Bering Strait submergence prior to the LGM reflects the correspondingly high uncertainty as to the history of GMSL leading up to the LGM. Estimates of GMSL between 50 and 30 ka from various geological and geochemical data range between −25 and −105 m (Fig. 2*B*, refs. (18–24)). This GMSL uncertainty of > 60 m, which exceeds the entire sea-level equivalent of the modern Antarctic Ice Sheet (58 m, (25)), reflects in part the paucity of geological sea-level observations: Advancing ice sheets razed evidence of prior ice margins (26), and sea-level rise during the last deglaciation destroyed or submerged ancient coastlines. In addition, radiometrically dated coral sea-level markers are limited to uplifted terraces during this time, with reconstructed paleo-elevations that are subject to errors in uplift corrections (27, 28).

The submergence history of the Bering Strait is important in diverse contexts. First, considering its modern sill depth of −53 m, the Bering Strait's submergence history, when corrected for glacial isostatic adjustment, could serve as a critically needed constraint on

Author contributions: J.R.F., T.P., and D.M.S. designed research; J.R.F., T.P., O.M.U., R.C.S., J.G., T.M.C., and F.F. performed research; J.R.F., T.P., and T.M.C. contributed new reagents/analytic tools; J.R.F., T.P., O.M.U., R.C.-S., J.G., F.F., A.M.-G., G.H.H., and D.M.S. analyzed data; and J.R.F., T.P., J.G., T.M.C., F.F., A.M.-G., G.H.H., and D.M.S. wrote the paper.

The authors declare no competing interest.

This article is a PNAS Direct Submission. C.W. is a guest editor invited by the Editorial Board.

Copyright © 2022 the Author(s). Published by PNAS. This open access article is distributed under Creative Commons Attribution-NonCommercial-NoDerivatives License 4.0 (CC BY-NC-ND).

[1]To whom correspondence may be addressed. Email: jesse.farmer@umb.edu or tpico@ucsc.edu.

[2]Present address: Department of Atmospheric Sciences, University of Washington, Seattle, WA 98195.

This article contains supporting information online at https://www.pnas.org/lookup/suppl/doi:10.1073/pnas.2206742119/-/DCSupplemental.

Published December 27, 2022.

Downloaded from https://www.pnas.org by 161.29.156.2 on December 27, 2022 from IP address 161.29.156.2.

GMSL between 50 and 30 ka. If RSL_{BeSt} is closely correlated with GMSL, sea-level inferences from the ICE-5G global ice sheet history (19) (black line, Fig. 2*B*), oxygen isotope records in the Red Sea (20) (red line, Fig. 2*B*), and a stacked sea-level equivalent oxygen isotope record (21) (blue line, Fig. 2*B*) suggest that the Bering Strait would have been subaerially exposed during this time, whereas recent GMSL estimates based on glacial isostatic adjustment analyses of sea-level data (22, 23) (purple line, Fig. 2*B*) and ice margin constraints (24) (gray line, Fig. 2*B*) indicate that the Bering Strait would have been submerged. Second, the Bering Strait's sea-level history impacts the connectivity of the Pacific and Atlantic Oceans, which has been hypothesized to control abrupt (millennial-scale) climate and ocean circulation variability during the last ice age (5, 6). Third, the submergence history affects when terrestrial migrations were possible between Asia and North America across the Bering Land Bridge, putatively leading to the first arrival of humans in North America.

Here, we reconstruct the history of Bering Strait submergence since 46 ka using a geochemical proxy for Pacific water input to the western Arctic Ocean (8) and simulations of relative sea level at the Bering Strait (11, 30). These reconstructions show that, contrary to previous assumptions (5, 6) and congruent with the original hypothesis of Hopkins (14), the Bering Strait was flooded by at least 46 ka and that the Bering Land Bridge formed only after ~36 ka.

The geochemical proxy for Bering Strait submergence is based on regional features of the marine nitrogen (N) cycle in the polar Northern hemisphere oceans. The N isotopic composition ($\delta^{15}N = [(^{15}N/^{14}N)_{sample}/(^{15}N/^{14}N)_{air} - 1] * 1000$) of nitrate ($NO_3^-$), the primary form of fixed N supplied to surface ocean ecosystems, varies by about 3 parts per thousand (3‰) among the high-latitude North Atlantic, North Pacific, and western Arctic Oceans today (Fig. 1*A*). Specifically, the $\delta^{15}N$ of nitrate supplied to the surface mixed layer is substantially higher in the western Arctic (~8‰) than in the eastern Arctic or subpolar North Atlantic (~5‰). The high western Arctic nitrate $\delta^{15}N$ arises from two features unique to the Pacific inflow across the Bering Strait. First, the nitrate inflow across the Bering Strait is elevated in $\delta^{15}N$ relative to the high-latitude North Atlantic Ocean. This reflects both the higher nitrate $\delta^{15}N$ in subarctic North Pacific subsurface waters relative to subarctic North Atlantic waters (*SI Appendix*, Fig. S1) due to water column denitrification in the North Pacific interior, and partial nitrate assimilation in Bering Sea surface waters (32). Second, the high nitrate concentration of this Bering Strait inflow fuels high shelf productivity, which in turn initiates coupled partial nitrification-denitrification (CPND) on the Bering Sea shelf and the western Arctic shelves; this CPND further elevates nitrate $\delta^{15}N$ (33–36). Importantly, the Arctic Ocean's CPND is sited exclusively in areas that are influenced by the Bering Strait inflow (33–36) (*SI Appendix*, section S2 and Figs. S1 and S2). Accordingly, the subsurface nitrate $\delta^{15}N$ elevation in the western Arctic is directly tied to Pacific nitrate input (Fig. 1*A*).

We reconstruct the N isotope signature associated with the Bering Strait inflow back to 46 ka by measuring the $\delta^{15}N$ of organic matter bound within the planktonic foraminifer *Neogloboquadrina pachyderma* (hereafter, $\delta^{15}N_{N.p.}$) from three sediment cores in the western Arctic Ocean and, as a control, from one core in the central Arctic Ocean outside the direct influence of the Bering Strait inflow (Fig. 1*A*). Planktonic foraminifera-bound $\delta^{15}N$ (such as $\delta^{15}N_{N.p.}$) reflects the $\delta^{15}N$ of organic matter produced in surface waters (8, 37), which depends on the $\delta^{15}N$ of the subsurface nitrate supply and the degree of nitrate consumption, that is, the summertime drawdown of nitrate as a proportion of annual nitrate supply (38). Summertime nitrate consumption is complete in the western Arctic today due to the highly stratified upper water column (39), which arises in part from continual supply of low-salinity seawater across the Bering Strait (8) (Fig. 1).

Farmer et al. (8) showed that western Arctic $\delta^{15}N_{N.p.}$ recorded the most recent postglacial flooding of the Bering Strait, which has been dated by independent methods to 13 to 11 ka (e.g., refs. (11) and (12)) (Fig. 2*D*). During Marine Isotope Stage (MIS) 2 (29 to 11.7 ka, including the LGM), western Arctic $\delta^{15}N_{N.p.}$ ranged from 4.5 to 6‰, requiring Atlantic-sourced nitrate as well as incomplete nitrate consumption due to weaker density stratification (8). Around 11.5 ka, western Arctic $\delta^{15}N_{N.p.}$ rapidly rose to values of 7.8 to 8.8‰ throughout the Holocene. This $\delta^{15}N_{N.p.}$ rise resulted from flooding of the Bering Strait, which introduced nitrate-rich, high-$\delta^{15}N$ Pacific waters, triggered shelf

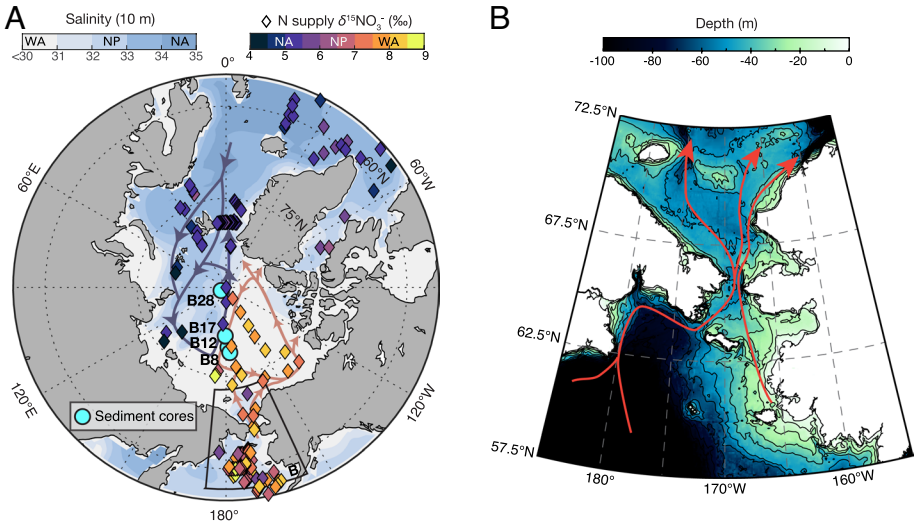

Fig. 1. Hydrography of the polar Northern Hemisphere and Bering Strait bathymetry. (*A*) Mixed layer (10 m depth) salinity (7) (blue shading) and subsurface (~50 to 200 m) nitrogen isotopic composition ($\delta^{15}N$) of nitrate (diamonds). From published data sets, sample depths were chosen to capture the nitrate being supplied to the mixed layer in the Arctic and North Atlantic (NA), and the North Pacific (NP) nitrate being transported across the Bering Strait (see data sources and selection criteria in *SI Appendix*, section S2). The mean salinity and nitrate $\delta^{15}N$ values for the western Arctic (WA), NP, and NA are indicated on the color bars. Cyan circles show locations of sediment cores; light blue and orange arrows show schematic circulation of Atlantic- and Pacific-sourced nitrate-rich subsurface waters, respectively (8, 9). (*B*) Bering Strait bathymetry (1) contoured at 10 m intervals. Red lines indicate principal ocean transport pathways (10).

Downloaded from https://www.pnas.org by 161.29.156.2 on December 27, 2022 from IP address 161.29.156.2.

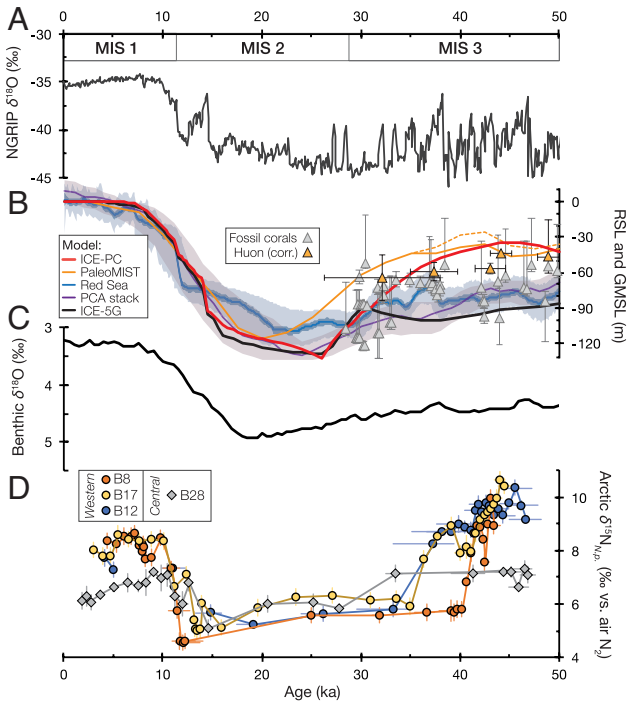

Fig. 2. Arctic Ocean foraminifera-bound N isotope records compared with related records of climate and sea-level change since 50 ka. (*A*) NGRIP ice core δ^{18}O, reflecting Greenland air temperature (29). (*B*) Sea-level reconstructions from ICE-5G (19) (black), the Red Sea (20) (blue-red shading), stacked oxygen isotope-based sea-level reconstructions (21) (purple with purple shading), PaleoMIST (24) (orange, dashed line is minimal MIS 3 GMSL scenario), ICE-PC (red, this study and ref. (30)), previously published MIS 3 coral sea-level benchmarks (27) (gray triangles), and recently corrected Huon Peninsula sea-level datums (28) (yellow triangles). (*C*) Global benthic foraminifera δ^{18}O stack (31), which records both global ice volume and deep ocean temperature and is widely applied as a sea-level proxy. (*D*) Western (circles) and central (gray diamonds) Arctic Ocean $\delta^{15}N_{N.p.}$ (this study); vertical error bars denote the larger of measured or long-term replicate $\delta^{15}N_{N.p.}$ precision (*Methods*), and horizontal error bars denote 68% quantiles (equivalent to ±1sd) of the age-depth model. Timing of MIS 1 to 3 according to (31) is denoted at the top.

CPND that further elevated nitrate δ^{15}N in the western Arctic, and stratified the upper water column, leading to complete nitrate consumption (8).

New $\delta^{15}N_{N.p.}$ records from three western Arctic Ocean sediment cores extend these reconstructions to the limit of radiocarbon dating (~50 ka), through the pre-LGM interval of larger sea-level uncertainty (Fig. 2). Results exhibit three distinct intervals separated by two rapid transitions. The youngest transition, a $\delta^{15}N_{N.p.}$ rise of ~3‰ around 11 ka, records the postglacial flooding of the Bering Strait discussed above, ending the low $\delta^{15}N_{N.p.}$ (of 4.5 to 6‰) of MIS 2. The new data show that the low $\delta^{15}N_{N.p.}$ of MIS 2 did not extend back through MIS 3 (57 to 29 ka). Instead, all the three western Arctic sites show high $\delta^{15}N_{N.p.}$ values of 8 to 10.5‰ prior to 35 to 40 ka; these values are equivalent to or higher than Holocene $\delta^{15}N_{N.p.}$ at these locations. Moreover, western Arctic $\delta^{15}N_{N.p.}$ values are 2 to 3.5‰ higher than those measured in the central Arctic before 35 to 40 ka (Fig. 2*D*). Western and central Arctic $\delta^{15}N_{N.p.}$ values converge after 35 ka, with similar $\delta^{15}N_{N.p.}$ values (of 4.5 to 6‰) lasting in both regions until 11 ka.

Moving forward in time from MIS 3, all the three western Arctic cores show a ~3‰ $\delta^{15}N_{N.p.}$ decline within 2 cm of sediment (equating to 1 to 2 kyr based on age models; *SI Appendix*, section S1 and Fig. S3). Radiocarbon age models (*SI Appendix*, Fig. S3) date this transition to 40 ka at B8 and 35 ka at B12 and B17 (*SI Appendix*, Fig. S5*A*). The data are consistent with a simultaneous $\delta^{15}N_{N.p.}$ decline in all the three cores, given the age model uncertainties of up to ±3 ka (95% CI) (*SI Appendix*, Fig. S5) and also considering the potential effects of bioturbation at these low sedimentation rates. Conversely, it would be difficult to explain different timings in the large and similar magnitude of $\delta^{15}N_{N.p.}$ decline at these three proximal western Arctic cores (which are all located within 360 km of one another; Fig. 1*A*). Moreover, true diachrony in the $\delta^{15}N_{N.p.}$ decline among sites is inconsistent with the decline in $\delta^{15}N_{N.p.}$ occurring first at Site B8, which is the site closest to the Bering Strait (Fig. 1*A*) and so would presumably be the last site to lose an isotopic signal emanating from the Strait. Thus, we consider that the $\delta^{15}N_{N.p.}$ decline is contemporaneous at these locations and assign a median (± interquartile range) age for the transition of $35.7^{+3.3}_{-2.4}$ ka (*SI Appendix*, Fig. S5*A*).

The MIS 3 western Arctic $\delta^{15}N_{N.p.}$ records require the presence of a high-δ^{15}N nitrate source that was rapidly removed around 36 ka. A terrigenous N source can be excluded, as both dissolved and particulate nitrogen inputs from Arctic rivers are too low in δ^{15}N [2 to 5‰; (40, 41)] to explain the elevated western Arctic $\delta^{15}N_{N.p.}$ values. This is also supported by low nitrate δ^{15}N (<5‰) in the Kara Sea and the Laptev Sea, where large terrigenous N contributions are expected (Fig. 1*A* and *SI Appendix*, Fig. S2). Additionally, our central Arctic $\delta^{15}N_{N.p.}$ record (gray diamonds in Fig. 2*D*) requires that the high-δ^{15}N nitrate was limited to the western Arctic during MIS 3, as occurs today (Fig. 1). The central Arctic $\delta^{15}N_{N.p.}$ record averages 7.1‰ prior to 35 ka; this value is consistent with foraminifera-bound δ^{15}N records from the North Atlantic that indicate a regional upper water column nitrate δ^{15}N of 5 to 6‰ during MIS 3 (42). Thus, the central Arctic most likely received nitrate from the North Atlantic Ocean during MIS 3, as occurred throughout the last 35 kyr (8). The $\delta^{15}N_{N.p.}$ homogeneity of the western and central Arctic between 35 and 11 ka (Fig. 2*D*) points to similar North Atlantic nitrate sources and a shared condition of weak upper ocean stratification in the two regions (8). Finally, the spatial gradient in $\delta^{15}N_{N.p.}$ between the western and central Arctic that occurred prior to ~36 ka redeveloped by 11 ka with the deglacial flooding of the Bering Strait. Thus, from an N isotopic perspective, MIS 3 and the Holocene appear remarkably similar in the Arctic (Fig. 2).

Given the above evidence, we conclude that the Bering Strait was flooded prior to ~36 ka. With a flooded Bering Strait, high-δ^{15}N nitrate from the Bering Sea would have been transported northward into the western Arctic Ocean as occurs today (33–36) (*SI Appendix*, Fig. S2). High nutrient concentrations in these Bering Strait inflow waters would also have fueled high primary productivity at the shelf break, triggering CPND that further elevates nitrate δ^{15}N in the western Arctic today (Fig. 1 and *SI Appendix*, section S3 and Fig. S1*D*). Finally, nitrate consumption in the western Arctic is complete due to the strong density stratification of the region, which appears contingent on the low-salinity Bering Strait inflow (8). The existence of this inflow before 36 ka may have strengthened western Arctic stratification at that time, leading to more complete surface ocean nitrate consumption in the western Arctic, and this may be required to reach the high $\delta^{15}N_{N.p.}$ of MIS 3.

It is noteworthy that western Arctic $\delta^{15}N_{N.p.}$ is higher between 40 and 46 ka than during the Holocene. This could reflect a greater extent of halocline and surface waters influenced by the Bering Strait inflow in the former period, enhanced CPND on the Bering Sea and western Arctic shelves, and/or a higher δ^{15}N of the subarctic North Pacific nitrate source flowing onto the Bering Sea shelf due to more complete summertime nitrate consumption in the Bering Sea, as suggested by higher diatom-bound δ^{15}N in the Bering Sea during MIS 3 (43). While our current data do not distinguish among these explanations, a flooded Bering Strait during MIS 3 is required in all cases.

Downloaded from https://www.pnas.org by 161.29.156.2 on December 27, 2022 from IP address 161.29.156.2.

After ~36 ka, the rapid $\delta^{15}N_{N.p.}$ decline at all three western Arctic sites and $\delta^{15}N_{N.p.}$ values of <7‰ indicate the cessation of the Bering Strait inflow to the Arctic, following the same logic as outlined above (*SI Appendix*, section S3). This reflects the subaerial exposure of the Bering Strait and thus formation of the Bering Land Bridge, with a terrestrial connection persisting through the LGM (11, 12, 14, 17).

To assess the quantitative implications of our findings for global ice volume during MIS 3, we model glacial isostatic adjustment and relative sea level at the Bering Strait (RSL_{BeSt}). Our simulations assume that the modern sill depth of the Bering Strait (−53 m) has not substantially changed since 50 ka due to vertical displacement from processes unrelated to ice loading, such as longer term local tectonic, erosion, and sedimentation effects, as these are unlikely to be significant over the short time interval of our study (e.g., ref. (11)). We performed gravitationally self-consistent glacial isostatic adjustment simulations using three ice histories that encompass the range of MIS 3 GMSL estimates (Figs. 2*B* and 3*B*). The first ice history, ICE-5G (19), is characterized by MIS 3 GMSL values of −82 to −100 m (Fig. 3*B*). Peak predicted RSL_{BeSt} during mid-MIS 3 (50 to 35 ka) is −65 m, below the modern sill depth (−53 m, Fig. 3*C*). The second ice history is derived from a GMSL history constructed by scaling $\delta^{18}O$ records to coral reef sea-level records ((18); *Materials and Methods*) and is characterized by a GMSL of −71 to −62 m during mid-MIS 3. RSL_{BeSt} based on this ice history (18) predicts an exposed Bering Strait from 50 to 35 ka, with RSL_{BeSt} below or equal to the sill depth (−58 to −53 m) (Fig. 3*C*). In summary, neither of these ice volume reconstructions associated with canonical sea-level histories (18, 19) are consistent with our finding of a flooded Bering Strait during MIS 3.

Recent studies on the magnitude of GMSL during mid-MIS 3 (50 to 35 ka) suggest substantially higher peak GMSL compared with the previous reconstructions (22–24). We estimate RSL_{BeSt} for a set of ice histories consistent with these recent GMSL constraints. One important caveat to these alternative ice histories is that RSL_{BeSt} is sensitive to the nearby ice sheet history (specifically, the Cordilleran Ice Sheet (CIS)) (11, 30). The CIS extent during MIS 3 is poorly constrained by field data, representing a source of uncertainty (44) (*SI Appendix*, section S4). To address this, we simulate three cases of MIS 3 CIS geometry (large, intermediate, small; *SI Appendix*, section S4), each of which maintains the same ICE-PC-derived GMSL history (30). In all three simulations, the Bering Strait is flooded during MIS 3 until after ~34 ka (*SI Appendix*, Fig. S7). For the intermediate CIS history, RSL_{BeSt} is -11 to -20 m (yielding a water depth of 33 to 42 m; Fig. 3*C*) during mid-MIS 3. Our relative sea-level predictions suggest that a greater extent of the CIS results in a more deeply submerged Bering Strait (that is, a higher RSL_{BeSt}). Nevertheless, the three CIS geometries produce RSL_{BeSt} predictions that differ by less than 10 m (*Materials and Methods* and *SI Appendix*, Fig. S7). During MIS 3 and the LGM, glacial isostatic adjustment causes RSL_{BeSt} to be higher than GMSL by 20 to 30 m during MIS 3 and the LGM (compare Fig. 3 *B* and *C*). Nevertheless, our simulations show that GMSL changes are the dominant control on relative sea-level changes at the Bering Strait leading up to the LGM. Thus, a fully flooded Bering Strait during MIS 3 appears to require a global ice volume history in which MIS 3 ice volume is <50% (and in the case of ICE-PC, <30%) that of MIS 2 (22–24). This ice history contrasts with the long-dominant view of only modest ice retreat during MIS 3 (e.g., refs. (19–21)). A flooded Bering Strait before ~36 ka also requires that ice sheets grew quickly from MIS 3 until the LGM (Fig. 3*B*), consistent with previous findings (23, 45).

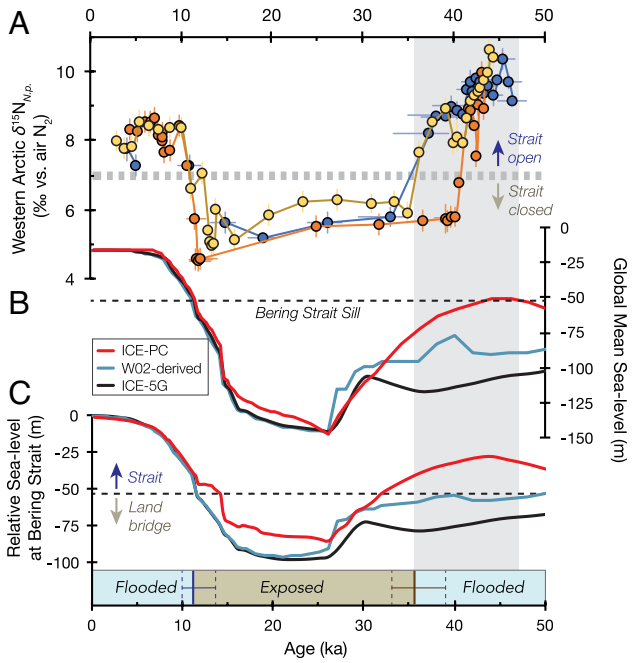

Fig. 3. Western Arctic Ocean $\delta^{15}N_{N.p.}$, global mean sea-level reconstructions, and glacial isostatic adjustment simulation of Bering Strait relative sea-level history. (*A*) Western Arctic Ocean $\delta^{15}N_{N.p.}$; dashed horizontal bar denotes maximum expected $\delta^{15}N_{N.p.}$ for an exposed Bering Strait (*Methods*). Vertical error bars denote the larger of measured or long-term replicate $\delta^{15}N_{N.p.}$ precision; horizontal error bars denote 68% quantiles (equivalent to ±1sd) of the age-depth model. (*B*) GMSL from ICE-5G (19) (black), from an ice history constructed from the pre-LGM GMSL in ref. (18) (W02-derived, blue), and from ICE-PC (red). (*C*) Relative sea level at the Bering Strait from ice volume histories in *B*, where ICE-PC RSL_{BeSt} is based on the intermediate Cordilleran Ice Sheet history (*Materials and Methods*). Black dashed line in *B* and *C* denotes modern sill depth of the Bering Strait (−53 m). Gray vertical shading denotes the timing of pre-LGM Bering Strait flooding reconstructed from panel (*A*). Colored bar at the bottom of *C* shows interpreted Bering Strait sea-level history. Brown vertical line denotes the reconstructed timing of Bering Strait closure in MIS 3; dashed brown lines are ±95% confidence intervals (this study). Blue vertical line and dashes denote the mean timing and range of observations for postglacial Bering Strait flooding, respectively (8, 11, 12).

Our Bering Strait submergence and GMSL reconstructions have implications for climate. First, relative sea level above −53 m at the Bering Strait until ~36 ka (Fig. 4*A*) supports recent estimates of peak MIS 3 GMSL near −40 m (22–24, 46, 47), indicating that peak MIS 3 global ice volumes were more similar to the Holocene than to the LGM (Fig. 4*B*). In contrast, global temperature proxies suggest that MIS 3 was notably colder than the Holocene and only slightly warmer than the LGM (Fig. 4*D*). If global temperatures during MIS 3 were indeed similar to the LGM, why was ice volume so much lower during MIS 3? The growth of ice volume in late MIS 3 might reflect nonlinearity in the sensitivity of ice volume to CO_2 radiative forcing (Fig. 4*E*), with ice volume responding more to CO_2 change when CO_2 is low and climate is cold (48). However, such nonlinearity would need to be very strong to explain the observations, with the radiative forcing from the decline in atmospheric CO_2 from 220 to 190 ppmv between 40 and 30 ka driving >60 m sea-level equivalent ice volume growth (Fig. 4 *B* and *E*). An alternative possibility is that Northern Hemisphere ice volume growth was more directly controlled by peak summer insolation than by global temperature (13, 24, 49), as supported by the coincidence of declining 65°N summer insolation (Fig. 4*C*) and increasing ice volume through late MIS 3 (Fig. 4*B*) despite relatively little global cooling (Fig. 4*D*). This distinction may indicate a strong role for local summer insolation in driving ice loss (Fig. 4 *B* and *C*), for example, by direct irradiance-driven ablation (e.g., ref. (50)) or as a local driver

Downloaded from https://www.pnas.org by 161.29.156.2 on December 27, 2022 from IP address 161.29.156.2.

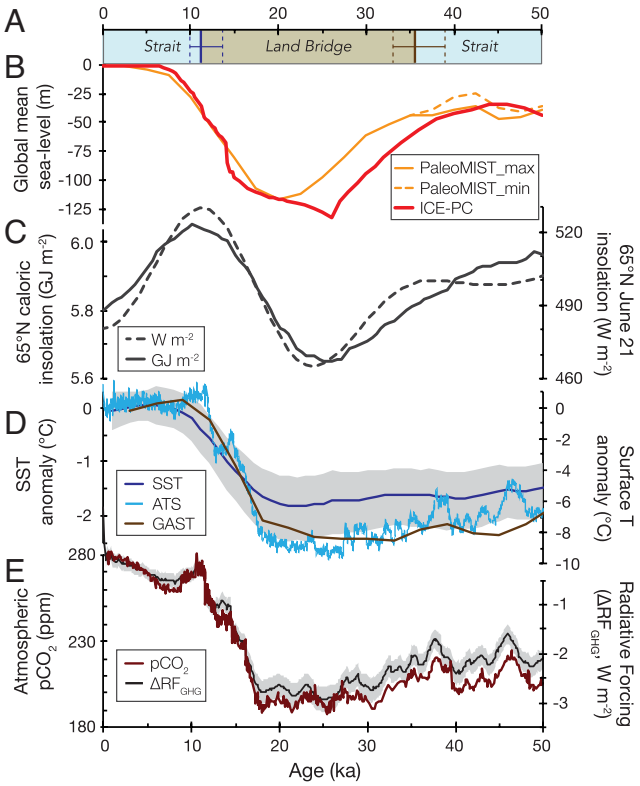

Fig. 4. Comparison of histories of Bering Strait flooding, sea level, climate, and climate forcings over the last 50 kyr. (*A*) Bering Strait and Bering Land Bridge intervals based on western Arctic $\delta^{15}N_{N.p.}$ (as in Fig. 3); (*B*) ICE-PC (this study, red) and PaleoMIST ((24), orange) sea-level reconstructions. (*C*) 65°N summer solstice mean daily insolation (dashed, W m^{-2}) and caloric summer half-year insolation (51) (solid, GJ m^{-2}). (*D*) Global average surface temperature anomaly (52) (brown), Antarctic ice core temperature stack (ATS) anomaly (53) (cyan), and global sea surface temperature (SST) anomaly (49) (blue, shading is 95% CI). (*E*) Atmospheric CO_2 concentration (54, 55) (dark red) and cumulative greenhouse gas (CO_2, CH_4, and N_2O) radiative forcing (56) (ΔRF_{GHG}; black, shading is ±1sd).

of summertime air temperature change over the Northern Hemisphere ice sheets.

Second, given the importance of ice albedo to global temperature, a complementary question emerges: If ice volume during MIS 3 was sufficiently low to allow for a flooded Bering Strait, then why was MIS 3 so cold? One possibility is that the radiative impact of low ice volume was compensated by spatially extensive but thin land ice and snow cover as well as sea ice during MIS 3 (49). The cold MIS 3 climate could also indicate an outsized importance of low atmospheric CO_2 concentrations during MIS 3 (200 to 220 ppmv, Fig. 4*E*) to Earth's radiative balance (49). In general, the deviation from linear correlation between climate and ice volume during MIS 3 provides a new test for models of climate and glaciation. Extending the use of the Bering Strait as a sea-level gauge further back in time will likely offer additional constraints on the mechanisms underlying the glacial cycles as glaciological and climatic phenomena.

Third, in both simple and fully coupled climate models, the Bering Strait's sea-level history contributes to the response of North Atlantic Deep Water production to regional freshwater perturbations (5, 6). These simulations led to the proposal that subaerial exposure of the Bering Strait was a prerequisite for the millennial-scale Northern hemisphere climate variability during the last glacial period (5, 6). However, our data indicate that millennial-scale variability in climate and ocean circulation occurred both when the Bering Strait was flooded (46 to 36 ka) and exposed (36 to 11.5 ka) (Fig. 2). Thus, closure of the Bering Strait was not needed for the occurrence of millennial-scale variability during the last ice age.

Finally, our reconstructed Bering Strait submergence history has implications for humans' arrival in the Americas. Recent evidence for human presence in North America between 23 and 21 ka (15) appears to require that humans migrated across Beringia before the onset of LGM conditions (15, 16). Limited regional archaeological records of human occupation before and during the LGM, particularly from eastern Beringia, preclude identification of the key factors controlling human migration at this time. However, comparison of our results with demographic age modeling of Beringian populations suggests one possibility. Humans were present in North Siberia as early as 45 ka (57), with a unique Ancient North Siberian population diverging from East Asians by 39 ka (95% CI 45.8 to 32.2 ka, ref. (58)). A second distinct Ancient Beringian population with direct ancestry to Native Americans emerged from East Asians at 36 ± 1.5 ka (16). Our data indicate that Siberia and Alaska were separated by the Bering Strait until the Bering Land Bridge formed at $35.7^{+3.3}_{-2.4}$ ka. Together, these findings suggest that, in the context of the last ~50 kyr, humans migrated into the Americas as soon as the Bering Land Bridge allowed for their passage. If correct, such simultaneity implies a strong drive for migration among the ice-age human populations in Siberia.

Materials and Methods

Three western Arctic cores were obtained from Mendeleev Ridge: Site B8 (78.13°N, 176.74°W, 1,031 m water depth), Site B12 (79.99°N, 174.29°W, 1,609 m water depth), and Site B17 (81.27°N, 178.97°E, 2,217 m water depth). The central Arctic core, Site B28, was obtained from Lomonosov Ridge (88.87°N, 140.18°E, 1,990 m water depth). Sediment samples were taken every 1 cm. Approximately 1,500 *Neogloboquadrina pachyderma* sinistral (Ehrenberg) tests (5 to 7 mg) were picked from the 150 to 300 μm size fraction under a binocular microscope. Foraminifera-bound nitrogen isotope analyses were performed at Princeton University following the procedures described in ref. (8), which are modified from refs. (59) and (60). Briefly, *N. pachyderma* samples were gently crushed; subjected to clay removal, reductive cleaning, and oxidative cleaning; dissolved in 4 N HCl to release bound organic nitrogen; oxidized to nitrate with basic potassium persulfate; and converted to N_2O gas via the denitrifier method (61). N isotopes were measured on N_2O with a custom-built, automated, helium continuous flow-based extraction and purification system coupled to a MAT253 isotope ratio mass spectrometer (62–64). The analytical precision based on long-term replication of internal carbonate-bound organic N standards is <±0.30‰ (1sd). The analytical precision of full procedural replicate $\delta^{15}N_{N.p.}$ analyses averaged ±0.22‰ (1sd, n = 42; error bars plotted on Figs. 2*D* and 3*A*). Further information on sediment core age models, constraints on the isotopic composition of nitrate in the polar Northern Hemisphere (Fig. 1*A*), and the interpretation of Bering Strait sea-level history from $\delta^{15}N_{N.p.}$ is provided in the *SI Appendix*, Texts S1–S3.

The growth and decay of ice sheets produces a complex sea-level change pattern as the solid Earth responds through crustal deformation, perturbations to the Earth's gravitational field, and changes to the Earth's rotation axis. Our gravitationally self-consistent sea-level calculations are based on the theory and pseudo-spectral algorithm of (65) with a spherical harmonic truncation at degree and order 256. These calculations include the impact of load-induced Earth rotation changes on sea level (66, 67), evolving shorelines, and the migration of grounded, marine-based ice (65, 68–70). Our numerical predictions require models for Earth's viscoelastic structure and the history of global ice cover. We use an Earth model characterized by a lithospheric thickness of 48 km, and an upper and lower mantle viscosity of 0.5×10^{21} Pa s and 5×10^{21} Pa s, respectively (as in ref. (11)). An evaluation of these results using an alternative Earth model (VM2) is provided in the *SI Appendix*, Text S4.

Our relative sea-level predictions for the Bering Strait additionally require global ice sheet histories to be input into the Earth model described above.

Downloaded from https://www.pnas.org by 161.29.156.2 on December 27, 2022 from IP address 161.29.156.2.

Here, we employ three ice sheet histories: ICE-5G, ICE-PC, and W02-derived (*SI Appendix*, Table S1). The ICE-5G ice history is from ref. (19). The ICE-PC ice history is from ref. (23) and is constrained such that the LGM and deglaciation (26 ka to 0 ka) global mean sea-level history is identical to the ICE-6G ice history (71), while the pre-LGM ice history is scaled to fit a global mean sea-level (GMSL) history based on fitting GMSL highstand constraints during MIS 3, MIS 5a, and MIS 5c (23). The W02-derived ice history is a global ice sheet history for which the deglacial ice sheet history is identical to the ICE-5G deglacial history (26 ka to 0 ka, ref. 15), while the glaciation phase (before 26 ka) adopts ice geometries based on Waelbroeck et al.'s GMSL history (18). Before 26 ka, the ice history at each time point is set by the GMSL history in ref. (18), with ice geometry assumed to be identical to the post-LGM ICE-5G ice history in the period with the same GMSL value. We note that the resultant GMSL history of the W02-derived ice history (Fig. 3*B*) is not identical to the originally published GMSL history of ref. (18). The Earth model is run using these three ice histories at 1 to 2 kyr timesteps.

Because the melt and growth history of the proximal Cordilleran Ice Sheet (CIS), and especially its rapid collapse events, can have a first-order effect on Bering Strait relative sea level (11), it is also essential to consider possible CIS geometries in modeling Bering Strait relative sea level. To address the sensitivity of Bering Strait relative sea level to the CIS, we test a suite of CIS ice sheet geometries, which incorporate what we term a small, intermediate, and large CIS. We produce a set of three ice histories corresponding to the ICE-PC GMSL history, which itself is based on the ICE-6G deglaciation history (71) (Fig. 3*B* and *SI Appendix*, Table S1). For the intermediate CIS (ICE-PC, Fig. 3*C*), the ice history's geographic distribution assumes that CIS ice geometry prior to 26 ka is identical to post-26 ka ice geometry for the same GMSL value based on ICE-6G deglaciation history (71). In contrast, for the large CIS (ICE-PC2), prior to 26 ka, the CIS maintains the same boundary as it had during the LGM, with its ice thickness scaled to fit the ICE-PC GMSL history (*SI Appendix*, Fig. S7). This large CIS, characterized by maximum ice extent, is part of a North American Ice Sheet history with a reduced MIS 3 eastern Laurentide Ice Sheet (23). For the small CIS (ICE-MIST), we adopt the CIS history (defined as west of 120° W, from 80 to 26 ka) from PaleoMIST (24). Each of these ice histories is characterized by an identical GMSL history (ICE-PC in Fig. 3*B*) that is maintained by changing ice thickness over Scandinavia and Antarctica, locations that are far-field to our site of interest at the Bering Strait. For the intermediate and large CIS history (ICE-PC and ICE-PC2), the deglaciation history (26 to 0 ka) is adopted from the GI-31 ice history (11, 30), and incorporates substantial melting of the North American ice sheet saddle, which connected the Cordilleran and Laurentide Ice Sheets, from 13 to 11.5 ka (*SI Appendix*, Table S1).

Data, Materials, and Software Availability. Foraminifera-bound N isotopes, sediment core age models, and sea level simulations data are included in the *SI Appendix*, Dataset S1.

ACKNOWLEDGMENTS. We thank Sergey Oleynik and Laura Gemery for laboratory assistance and Peter Huybers for discussions. J.R.F., D.M.S., and O.M.U. were supported by NSF OCE-2054780; J.R.F. was also supported by the Max Planck Society (with A.M.-G. and G.H.H.) and by the Tuttle Fund of the Department of Geosciences, Princeton University (with D.M.S.). T.P. was supported by NSF OCE-2054757. T.M.C. was funded by the United States Geological Survey Climate Research and Development Program. Any use of trade, firm, or product names is for descriptive purposes only and does not imply endorsement by the United States Government.

Author affiliations: [a]Department of Geosciences, Princeton University, Princeton, NJ 08544; [b]Max Planck Institute for Chemistry, Mainz 55128, Germany; [c]Earth and Planetary Sciences, University of California-Santa Cruz, Santa Cruz, CA 95064; [d]Department of Earth and Planetary Sciences, Harvard University, Cambridge, MA 02138; [e]Department of Marine Sciences, University of Connecticut, Groton, CT 06340; [f]Florence Bascom Geoscience Center, United States Geological Survey, Reston, VA 20192; [g]Department of Geosciences, Environment and Society, Université Libre de Bruxelles, Brussels 1050, Belgium; and [h]Department of Earth Sciences, ETH Zürich, Zürich 8092, Switzerland

1. S. L. Danielson *et al.*, Sounding the Northern Seas. *EOS* **96** (2015), 10.1029/2015EO040975.
2. R. A. Woodgate, Increases in the Pacific inflow to the Arctic from 1990 to 2015, and insights into seasonal trends and driving mechanisms from year-round Bering Strait mooring data. *Prog. Oceanogr.* **160**, 124–154 (2018).
3. A. Jahn, M. M. Holland, Implications of Arctic sea ice changes for North Atlantic deep convection and the meridional overturning circulation in CCSM4-CMIP5 simulations. *Geophs. Res. Lett.* **40**, 1206–1211 (2013).
4. M. Yamamoto-Kawai, E. Carmack, F. McLaughlin, Nitrogen balance and Arctic throughflow. *Nature* **443**, 43 (2006).
5. A. M. De Boer, D. Nof, The Bering Strait's grip on the northern hemisphere climate. *Deep Sea Res. Pt.* **51**, 1347–1366 (2004).
6. A. Hu *et al.*, Role of the Bering Strait on the hysteresis of the ocean conveyor belt circulation and glacial climate stability. *Proc. Natl. Acad. Sci. U.S.A.* **109**, 6417–6422 (2012).
7. S. K. Lauvset *et al.*, A new global interior ocean mapped climatology: The 1° x 1° GLODAP version 2. *Earth Syst. Sci. Data* **8**, 325–340 (2016), 10.5194/essd-8-325-2016.
8. J. R. Farmer *et al.*, Arctic Ocean stratification set by sea level and freshwater inputs since the last ice age. *Nat. Geosci.* **14**, 684–689 (2021), 10.1038/s41561-021-00789-y.
9. F. McLaughlin, E. Carmack, R. Macdonald, A. J. Weaver, J. Smith, The Canada Basin, 1989:1995: Upstream events and far-field effects of the Barents Sea. *J. Geophys. Res.* **107**, 3082 (2002).
10. S. L. Danielson *et al.*, Coupled wind-forced controls of the Bering-Chukchi shelf circulation and the Bering Strait throughflow: Ekman transport, continental shelf waves, and variations of the Pacific-Arctic sea surface height gradient. *Prog. Oceanogr.* **125**, 40–61 (2014).
11. T. Pico, J. X. Mitrovica, A. C. Mix, Sea level fingerprinting of the Bering Strait flooding history detects the source of the Younger Dryas climate event. *Sci. Adv.* **6**, eaay2935 (2020).
12. M. Jakobsson *et al.*, Post-glacial flooding of the Bering Land Bridge dated to 11 cal ka BP based on new geophysical and sediment records. *Clim. Past.* **13**, 991–1005 (2017), 10.5194/cp-13-991-2017.
13. P. U. Clark *et al.*, The last glacial maximum. *Science* **325**, 710–714 (1959).
14. D. M. Hopkins, Cenozoic history of the Bering land bridge. *Science* **129**, 1519–1528 (1959).
15. M. R. Bennett *et al.*, Evidence of humans in North America during the Last Glacial Maximum. *Science* **373**, 1528–1531. 10.1126/science.abg7586 (2021).
16. J. V. Moreno-Mayar *et al.*, Terminal Pleistocene Alaskan genome reveals first founding population of native Americans. *Nature* **553**, 203–207 (2018).
17. D. M. Hopkins, Sea level history in Beringia during the past 250,000 years. *Quat. Res.* **3**, 520–540 (1973).
18. C. Waelbroeck, L. Labeyrie, E. Michel, J. C. Duplessy, J. F. McManus, Sea-level and deep water temperature changes derived from benthic foraminifera isotopic records. *Quat. Sci. Rev.* **21**, 295–305 (2002).
19. W. R. Peltier, R. G. Fairbanks, Global glacial ice volume and last glacial maximum duration from an extended Barbados sea level record. *Quat. Sci. Rev.* **25**, 3322–3337 (2006).
20. K. M. Grant *et al.*, Rapid coupling between ice volume and polar temperature over the past 150,000 years. *Nature* **491**, 744–747 (2012), 10.1038/nature11593.
21. R. M. Spratt, L. E. Lisiecki, A late Pleistocene sea level stack. *Clim. Past* **12**, 1079–1092 (2016), 10.5194/cp-12-1079-2016.
22. T. Pico, J. X. Mitrovica, K. L. Ferrier, J. Braun, Global ice volume during MIS 3 inferred from a sea-level analysis of sedimentary core records in the Yellow River Delta. *Quat. Sci. Rev.* **152**, 72–79 (2016).
23. T. Pico, J. R. Creveling, J. X. Mitrovica, Sea-level records from the US mid-Atlantic constrain Laurentide ice sheet extend during marine isotope stage 3. *Nat. Commun.* **8**, 15612 (2017).
24. E. J. Gowan *et al.*, A new global ice sheet reconstruction for the past 80,000 years. *Nat. Commun.* **12**, 1199 (2021), 10.1038/s41467-021-21469-w.
25. P. Fretwell *et al.*, Bedmap2: Improved ice bed, surface and thickness datasets for Antarctica. *The Cryosphere* **7**, 375–393 (2013), 10.5194/tc-7-375-2013.
26. C. R. Stokes *et al.*, On the reconstruction of palaeo-ice sheets: Recent advances and future challenges. *Quat. Sci. Rev.* **125**, 15–49 (2015).
27. F. D. Hibbert *et al.*, Coral indicators of past sea-level change: A global repository of U-series dated benchmarks. *Quat. Sci. Rev.* **145**, 1–56 (2016).
28. de Gelder, G., Husson, L., Pastier, A.-M., Fernández-Blanco, D., Pico, T., Chauveau, D., Authemayou, C., & Pedoja, K. (2022). High interstadial sea levels over the past 420ka from the Huon Peninsula, Papua New Guinea. *Communications Earth & Environment*, **3**. https://doi.org/10.1038/s43247-022-00583-7
29. North Greenland Ice Core Project Members, High-resolution record of Northern hemisphere climate extending into the last interglacial period. *Nature* **431**, 147–151 (2004).
30. T. Pico, A. Robel, E. Powell, A. C. Mix, J. X. Mitrovica, Leveraging the Rapid Retreat of the Amundsen Gulf Ice Stream 13,000 Years Ago to Reveal Insight Into North American Deglaciation. *Geophys. Res. Let.* **46**, 12101–12107 (2019), 10.1029/2019GL084789.
31. L. E. Lisiecki, J. V. Stern, Regional and global benthic $d^{18}O$ stacks for the last glacial cycle. *Paleoceanography* **31**, 1368–1394 (2016).
32. Lehmann, M. F., Sigman, D. M., McCorkle, D. C., Brunelle, B. G., Hoffmann, S., Kienast, M., Cane, G., & Clement, J. (2005). Origin of the deep Bering Sea nitrate deficit: Constraints from the nitrogen and oxygen isotopic composition of water column nitrate and benthic nitrate fluxes. *Global Biogeochemical Cycles*, **19**(4), https://doi.org/10.1029/2005gb002508
33. J. Granger *et al.*, Coupled nitrification-denitrification in sediment of the eastern Bering Sea shelf leads to ^{15}N enrichment of fixed N in shelf waters. *J. Geophys. Res.* **116**, C11006 (2011).
34. J. Granger, D. M. Sigman, J. G. Gagnon, J.-E. Tremblay, A. Mucci, On the properties of the Arctic halocline and deep water masses of the Canada Basin from nitrate isotope ratios. *J. Gephys. Res. Oceans* **123**, 5443–5458 (2018).
35. F. Fripiat *et al.*, Influence of the bordering shelves on nutrient distribution in the Arctic halocline inferred from water column nitrate isotopes. *Limnol. Oceanogr.* **63**, 2154–2170 (2018).
36. Z. W. Brown, K. L. Casciotti, R. S. Pickart, J. H. Swift, K. R. Arrigo, Aspects of the marine nitrogen cycle of the Chukchi Sea shelf and Canada Basin. *Deep Sea Res. Pt.* **118**, 73–87 (2015).
37. H. Ren, D. M. Sigman, R. C. Thunell, M. G. Prokopenko, Nitrogen isotopic composition of planktonic foraminifera from the modern ocean and recent sediments. *Limnology and Oceanography*, **57**, 1011–1024 (2012). 10.4319/lo.2012.57.4.1011.
38. M. A. Altabet, R. Francois, Sedimentary nitrogen isotopic ratio as a recorder for surface ocean nitrate utilization. *Glob. Biogeochem. Cy.* **8**, 103–116 (1994).
39. A. Randelhoff *et al.*, Pan-Arctic Ocean primary production constrained by turbulent nitrate fluxes. *Front. Mar. Sci.* **7**, 150 (2020), 10.3389/fmars.2020.00150.
40. J. W. McClelland *et al.*, Particulate organic carbon and nitrogen export from major Arctic rivers. *Glob. Biogeochem. Cy.* **30**, 629–643 (2016), 10.1002/2015GB005351.
41. B. Thibodeau, D. Bauch, M. Voss, Nitrogen dynamic in Eurasian coastal Arctic ecosystem: Insight from nitrogen isotope. *Glob. Biogeochem. Cy.* **31**, 836–849 (2017).

Downloaded from https://www.pnas.org by 161.29.156.2 on December 27, 2022 from IP address 161.29.156.2.

42. M. Straub *et al.*, Changes in North Atlantic nitrogen fixation controlled by ocean circulation. *Nature* **501**, 200–203 (2013), 10.1038/nature12397.
43. B. G. Brunelle *et al.*, Evidence from diatom-bound nitrogen isotopes for subarctic Pacific stratification during the last ice age and a link to North Pacific denitrification changes. *Paleoceanography* **22**, PA1215 (2007).
44. J. Seguinot, I. Rogozhina, A. P. Stroeven, M. Margold, J. Kleman, Numerical simulations of the Cordilleran ice sheet through the last glacial cycle. *The Cryosphere* **10**, 639–664 (2016).
45. K. Lambeck, H. Rouby, A. Purcell, Y. Sun, M. Sambridge, Sea level and global ice volumes from the Last Glacial maximum to the holocene. *Proc. Natl. Acad. Sci. U.S.A.* **111**, 15296–15303 (2014), 10.1073/pnas.1411762111.
46. A. S. Dalton *et al.*, Was the Laurentide ice sheet significantly reduced during marine isotope stage 3? *Geology* **47**, 111–114 (2019), 10.1130/G45335.1.
47. C. L. Batchelor *et al.*, The configuration of Northern hemisphere ice sheets through the quaternary. *Nat. Commun.* **10**, 3713 (2019), 10.1038/s41467-019-11601-2.
48. P. Liautaud, P. Huybers, Increased sea level sensitivity to CO_2 forcing across the middle pleistocene transition from ice-albedo and ice-volume nonlinearities. *J. Clim.* **34**, 9693–9708 (2021), 10.1175/jcli-d-21-0192.1.
49. J. D. Shakun, D. W. Lea, L. E. Lisiecki, M. E. Raymo, An 800-kyr record of global surface ocean $\delta^{18}O$ and implications for ice volume-temperature coupling. *Earth Planet. Sci. Lett.* **426**, 58–68 (2015).
50. M. Suwa, M. L. Bender, Chronology of the Vostok ice core constrained by O_2/N_2 ratios of occluded air, and its implication for the Vostok climate records. *Quat. Sci. Rev.* **27**, 1093–1106 (2008).
51. P. C. Tzedakis, M. Crucifix, T. Mitsui, E. W. Wolff, A simple rule to determine which insolation cycles lead to interglacials. *Nature* **542**, 427–432 (2017), 10.1038/nature21364.
52. C. W. Snyder, Evolution of global temperature over the past two million years. *Nature* **538**, 226–228 (2016), 10.1038/nature19798.
53. F. Parrenin *et al.*, Synchronous change of atmospheric CO_2 and Antarctic temperature during the last deglacial warming. *Science* **339**, 1060–1063 (2013), 10.1126/science.1226368.
54. E. Monnin *et al.*, Evidence for substantial accumulation rate variability in Antarctica during the Holocene, through synchronization of CO_2 in the Taylor Dome, Dome C and DML ice cores. *Earth Planet. Sci. Lett.* **224**, 45–54 (2004).
55. T. K. Bauska, S. A. Marcott, E. J. Brook, Abrupt changes in the global carbon cycle during the last glacial period. *Nat. Geosci.* **14**, 91–96 (2021).
56. P. Köhler, C. Nehrbass-Ahles, J. Schmitt, T. F. Stocker, H. Fischer, A 156 kyr smoothed history of the atmospheric greenhouse gases CO_2, CH_4, and N_2O and their radiative forcing. *Earth Syst. Sci. Data* **9**, 363–387 (2017), 10.5194/essd-9-363-2017.
57. V. V. Pitulko *et al.*, Early human presence in the Arctic: Evidence from 45,000-year-old mammoth remains. *Science* **351**, 260–263 (2016), 10.1126/science.aad0554.
58. M. Sikora *et al.*, The population history of northeastern Siberia since the Pleistocene. *Nature* **570**, 182–188 (2019), 10.1038/s41586-019-1279-z.
59. A. N. Knapp, D. M. Sigman, F. Lipschultz, N isotopic composition of dissolved organic nitrogen and nitrate at the Bermuda Atlantic time-series study site. *Global Biogeochem. Cycles* **19**, GB1018 (2005).
60. H. Ren *et al.*, Foraminiferal isotope evidence of reduced nitrogen fixation in the ice age Atlantic Ocean. *Science* **323**, 244–248 (2009).
61. D. M. Sigman *et al.*, A bacterial method for the nitrogen isotopic analysis of nitrate in seawater and freshwater. *Anal. Chem.* **73**, 4145–4153 (2001).
62. K. L. Casciotti, D. M. Sigman, M. G. Hastings, J. K. Böhlke, A. Hilkert, Measurement of the oxygen isotopic composition of nitrate and seawater and freshwater using the denitrifier method. *Anal. Chem.* **74**, 4905–4912 (2002).
63. M. R. McIlvin, K. L. Casciotti, Technical updates to the bacterial method for nitrate isotopic analyses. *Anal. Chem.* **83**, 1850–1856 (2011).
64. M. A. Weigand, J. Foriel, B. Barnett, S. Oleynik, D. M. Sigman, Updates to instrumentation and protocols for isotopic analysis of nitrate by the denitrifier method. *Rapid Commun. Mass Spectrom.* **30**, 1365–1383 (2016).
65. R. A. Kendall, J. X. Mitrovica, G. A. Milne, On post-glacial sea level – II. Numerical formulation and comparative results on spherically symmetric models. *Geophys. J. Int.* **161**, 679–706 (2005), 10.1111/j.1365-246X.2005.02553.x.
66. G. Milne, J. X. Mitrovica, Postglacial sea-level change on a rotating Earth: First results from a gravitationally self-consistent sea-level equation. *Geophys. J. Int.* **126**, F13–F20 (1996).
67. J. X. Mitrovica, J. Wahr, I. Matsuyama, A. Paulson, The rotational stability of an ice-age earth. *Geophys. J. Int.* **161**, 491–506 (2005).
68. P. Johnston, The effect of spatially non-uniform water loads on prediction of sea-level change. *Geophys. J. Int.* **114**, 615–634 (1993).
69. K. Lambeck, A. Purcell, P. Johnston, M. Nakada, Y. Yokoyama, Water-load definition in the glacio-hydro-isostatic sea-level equation. *Quat. Sci. Rev.* **22**, 309–318 (2003).
70. G. A. Milne, J. X. Mitrovica, J. L. Davis, Near-field hydro-isostasy: The implementation of a revised sea-level equation. *Geophys. J. Int.* **139**, 462–482 (1999).
71. W. R. Peltier, D. F. Argus, R. Drummond, Space geodesy constrains ice age terminal deglaciation: The global ICE-6G_C (VM5a) model. *J. Gephys. Res. Solid Earth* **120**, 450–487 (2015), 10.1002/2014JB011176.

Downloaded from https://www.pnas.org by 161.29.156.2 on December 27, 2022 from IP address 161.29.156.2.